KYBERNETIKA — VOLUME *43* (2007), NUMBER 6, PAGES 817 – 829

# COUNTING NUMBER OF CELLS AND CELL SEGMENTATION USING ADVECTION–DIFFUSION EQUATIONS

Peter Frolkovič, Karol Mikula, Nadine Peyriéras and Alex Sarti

We develop a method for counting number of cells and extraction of approximate cell centers in 2D and 3D images of early stages of the zebra-fish embryogenesis. The approximate cell centers give us the starting points for the subjective surface based cell segmentation. We move in the inner normal direction all level sets of nuclei and membranes images by a constant speed with slight regularization of this flow by the (mean) curvature. Such multi-scale evolutionary process is represented by a geometrical advection-diffusion equation which gives us at a certain scale the desired information on the number of cells. For solving the problems computationally we use flux-based finite volume level set method developed by Frolkovič and Mikula in [3] and semi-implicit co-volume subjective surface method given in [1, 5, 6]. Computational experiments on testing and real 2D and 3D embryogenesis images are presented and the results are discussed.

*Keywords:* image processing, partial differential equations, nonlinear advection-diffusion equations, flux-based level set method, subjective surface method, embryogenesis

*AMS Subject Classification:* 35K55, 74S10, 92C55, 92C37

## 1. INTRODUCTION

In this paper we describe an application of the geometrical advection-diffusion equations to extraction of the important information from 2D and 3D embryogenesis images. Namely, we develop a method for counting number of cells in 2D and 3D images and consequently for extraction of approximate cell centers. The approximate cell centers give the starting points for the subjective surface based cell segmentation.

Either 2D or 3D nuclei or membranes images taken by a multi-photon laser microscopy at early stages of zebra-fish embryogenesis are represented by the image intensity functions, which we denote $u_n^0$ in case of nuclei and $u_m^0$ in case of membranes. Although nuclei and membranes images are color (either red or green in our case, cf. Figure 1), only one of the color channels is nonzero. So both $u_m^0, u_n^0$ can be understood as a scalar functions from an image domain $\Omega$, $\Omega \subset \mathbb{R}^2$ or $\Omega \subset \mathbb{R}^3$ to $\mathbb{R}$

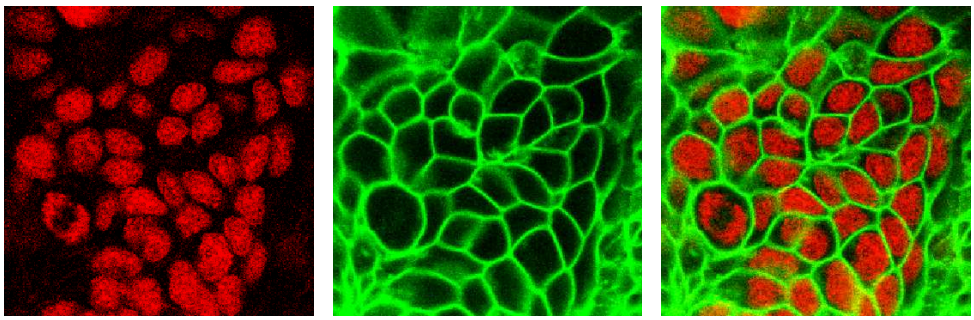

**Fig. 1.** 2D images of nuclei (left,red) and membranes (middle,green) taken by multi-photon laser microscopy. Combination of both images (right) showing the structure of cells in one particular 2D slice.

representing a "grey-level" image intensities. Without lost of generality we assume that $0 \leq u_n^0, u_m^0 \leq 1$.

The nuclei and membranes images have a specific feature that can be utilized for our goals. Namely, nuclei are given by (highly noisy) humps of the function $u_n^0$, and, inner parts of cells bounded by cell membranes are given by (highly noisy) humps of the function $1 - u_m^0$, see Figure 1 and Figure 2 top raw. Both these functions can be decomposed into level sets which can be further processed by properly designed geometrical advection-diffusion equations. To reach our goals we construct the evolutionary process (in the form of partial differential equation) which modifies their level sets (and correspondingly the functions themselves) utilizing their geometrical properties like direction of the normal vector field and the local curvature.

One can clearly observe that humps (representing either nuclei or inner part of cells) in the functions $u_n^0$ and $1 - u_m^0$ are composed by level sets with relatively large diameter $r_1$, $0 << c_1 \leq r_1 \leq c_2$, while diameter $r_2$ of level sets representing a noise is much smaller, close to zero, $0 < r_2 << c_1$. In order to extract approximate nucleus or cell centers we can evolve all level sets of $u_n^0$ or $1 - u_m^0$ in the inner normal direction by a constant speed. In general, the level sets are either closed curves (in 2D images) or closed surfaces (in 3D images), and, if they are moving in direction of inner normal vector field the encompassing area (volume) is decreasing and finally they disappear. However, the level sets with a small diameter, representing a noise, disappear (shrink) in a fast way, while level sets representing real image objects "live" for much longer time during such evolution (they are observable in long time-scales). Due to disappearing of the noise in a short scale we observe an intermediate state of evolution as shown in Figure 2 middle raw. The initial function is evolving and "filtered" (or denoised) due to shrinking of noisy level sets. It is also well-known that if the evolution of curves or surfaces depends on the local (mean) curvature then a speed of shrinking tends to infinity as diameter of level set tends to zero, cf. e. g. [4]. This fact is used in the so-called "curvature filters". So, in order to even speed up denoising in the above mentioned mechanism we can use additional slight dependence of the evolution of $u_n^0$ and $1 - u_m^0$ on the local curvature of their

level sets. In such case the evolutionary process can be represented by a geometrical equation

$$V = \delta + \mu k\,, \tag{1}$$

where the normal velocity $V$ of any level set is given by a constant $\delta$ plus the mean curvature $k$ multiplied by a positive constant $\mu$.

However, as mentioned above, we do not want to treat the level sets separately but all at once. Then the so-called level set formulation of equation (1) is very useful model [7]. It is given by the following geometrical advection-diffusion equation

$$\partial_t u = \delta \frac{\nabla u}{|\nabla u|} \cdot \nabla u + \mu |\nabla u| \nabla \cdot \left( \frac{\nabla u}{|\nabla u|} \right), \tag{2}$$

which can be applied to the initial conditions $u_n^0$ and $1 - u_m^0$, respectively. In both cases during the evolution the solution is shrinking and smoothed as shown in Figure 2 or Figure 4. We can also observe that the number of local maxima is fast decreasing in the beginning of the process, and, that there exists a period of time (a range of scales) when this number is stabilized. Solving equation (2) numerically (we explain our method in Appendix) we can find the number of local maxima and their spatial positions in every time step. If we observe no decrease in the number of local maxima in several subsequent time steps we stop the evolutionary process. The positions of the local maxima at this time-scale give us the approximate nuclei and cell centers. Counting of them give us an estimate on the number of cells in embryogenesis images. Applying this strategy to 3D image sequences can give us the rate of growth of the number of cells, and, finding correspondences between approximate cell centers can give us a specific representation of their morphogenesis. Moreover the spatially precise cell segmentation can be done using membranes images by the subjective surface method.

When the approximate cell centers are extracted we can construct automatically an initial peak-like profile of a segmentation function for each cell. Then, in order to extract the cell shapes, we can evolve every initial segmentation function using the subjective surface equation [8, 9]

$$\partial_t u = \sqrt{\varepsilon^2 + |\nabla u|^2} \nabla . \left( g(|\nabla G_\sigma * u_m^0|) \frac{\nabla u}{\sqrt{\varepsilon^2 + |\nabla u|^2}} \right). \tag{3}$$

Let us note that the equation can be solved in parallel for different (families of) cells using a parallel computational strategies. Since the solution of the equation (3) tends to a shock profile we can easily extract the cell boundary taking proper isoline (in 2D) and isosurface (in 3D), cf. Figure 6. Equation (3) has similar structure as the mean curvature part of the advection-diffusion equation (2). However, now the mean curvature driven motion is influenced by the edge indicator function $g(s) = 1/(1 + s^2)$ applied to (a smoothed by the Gaussian kernel) intensity $u_m^0$ of the membranes image. We are also free in choosing the parameter $\varepsilon$ coming from the Evans and Spruck regularization used in theoretical analysis of the mean curvature flow models [2]. Here, the parameter $\varepsilon$ shifts the model from the Riemannian mean curvature flow of level sets of $u$ ($\varepsilon = 0$) to the Riemannian mean curvature flow of

the graph of $u$ ($\varepsilon = 1$), cf. [9]. Let us note that the Evans and Spruck regularization with small $\varepsilon$ is used in denominators of equation (2) as well.

Since the equations (2) and (3) are both nonlinear geometric advection-diffusion partial differential equations we use the same numerical strategies to solve them, namely the semi-implicit finite volume schemes developed in [1, 3, 4, 5, 6]. Our computational methods are presented in Appendix. In the next sections we discuss their application to the cell number counting and segmentation.

## 2. EXTRACTION THE NUMBER OF CELLS AND APPROXIMATE CELL CENTERS

Let us choose first a relatively good detail (260 × 260 pixels) of a 2D slice from the zebra-fish embryogenesis image series. Majority of nuclei and membranes are well observable and the membranes image corresponds well to the nuclei one, see Figure 1. The graph of functions $u_n^0$ and $1-u_m^0$, respectively, are plotted in Figure 2 top. First, the function $u_n^0$ is used as initial condition and we applied equation (2) using parameters $\delta = 1$, $\mu = 0.0025$ and $\varepsilon = 10^{-3}$. In all our computations, the spatial step (pixel/voxel size) is equal to 0.01 and here we chose the time step $\tau = 0.0025$. We stopped the evolutionary process when the number of local maxima did not decrease in five subsequent time steps. In this experiment it occurred in 48th time step and number of detected nuclei was equal to 51. The resulting solution is plotted in Figure 2 middle left. The positions of detected approximate nuclei centers are superimposed to greyscale image in Figure 2 bottom left. Next we applied the same strategy to the function $1 - u_m^0$. In this case we used the same parameters but $\mu = 0.025$ (i. e., the result was obtained slightly increasing the mean curvature flow type diffusion). The process was stopped in 62 time step and the number of detected local maxima was 55. The resulting solution is plotted in Figure 2 middle right. The positions of detected approximate cell centers are superimposed to the greyscale image in Figure 2 bottom right.

Further example is given by 2D nuclei image with resolution 512 × 512 pixels chosen from the more noisy series. We used parameters $\delta = 1$, $\mu = 0.025$, $\varepsilon = 10^{-3}$ and $\tau = 0.0025$. In this slice we detected 91 nuclei centers after 40 time steps, the results are plotted in Figure 3.

In 3D case we first tested the method using an artificial 3D phantom image with resolution $100^3$ voxels, see Figure 4 top. We built 125 spheres with centers located on a grid inside the 3D image and with randomly generated radii from $4h$ to $10h$, where $h$ is a voxel size. Then we added different type and level of noise and tested number of spheres detected by the algorithm with very promising results. As an illustration, in Figure 4 middle and bottom rows, we show experiment where we put 50 % additive noise to 50 % of randomly chosen voxels and salt-and-pepper noise with range [0,0.5] to 10 % of randomly chosen voxels. 125 spheres were detected and the evolution of solution in central slice is shown, where one can clearly see correct 25 local maxima after process stabilization. For the artificial 3D testing examples we used parameters $\delta = 1$, $\mu = 0.00125$, $\varepsilon = 10^{-3}$ and $\tau = 0.00125$.

In the next real 3D example we consider volume containing 30 slices in z-direction,

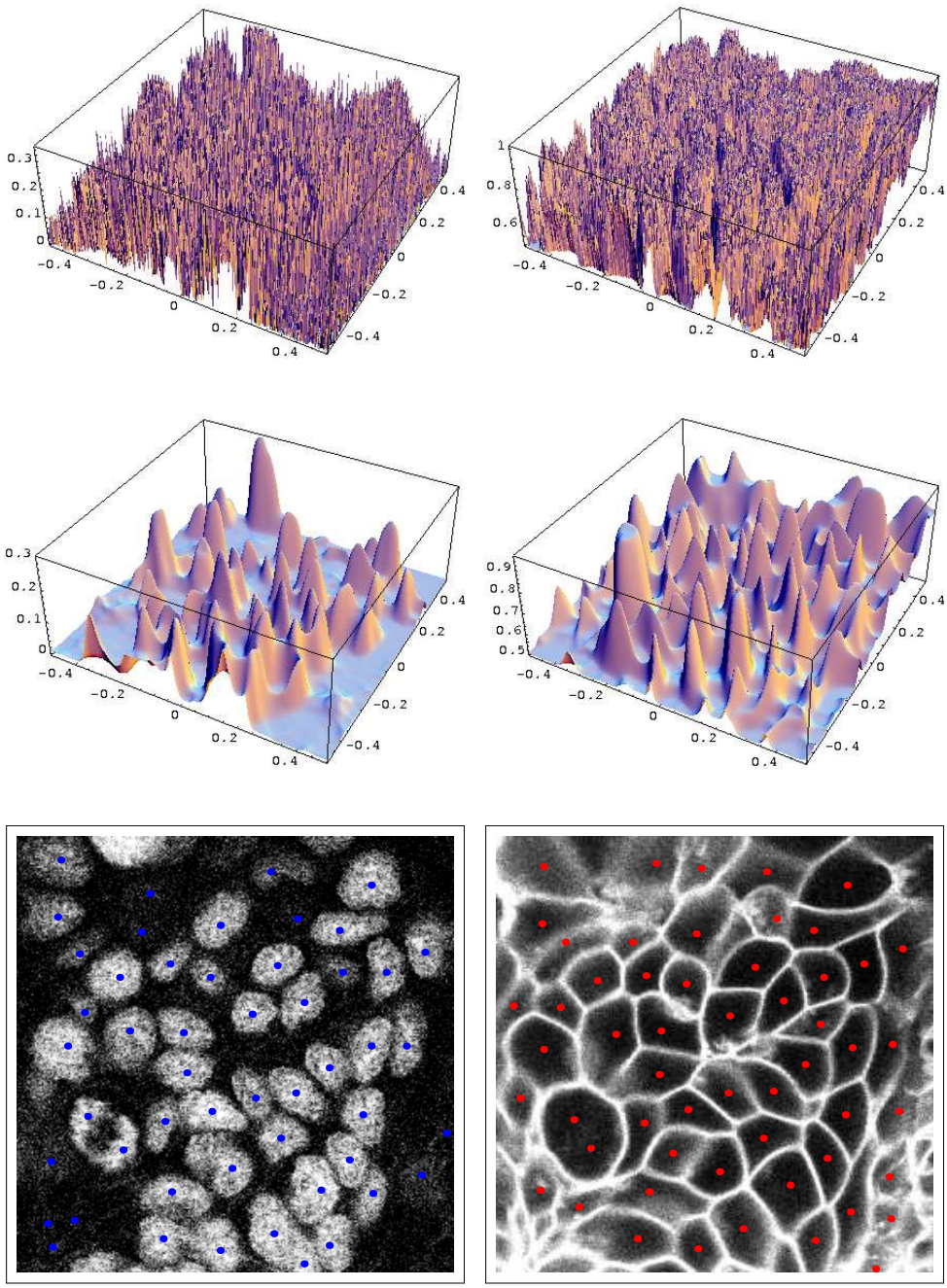


**Fig. 2.** Examples of detecting approximate nuclei and cell centers in 2D embryogenesis images using the flux-based level set method applied to equation (2).

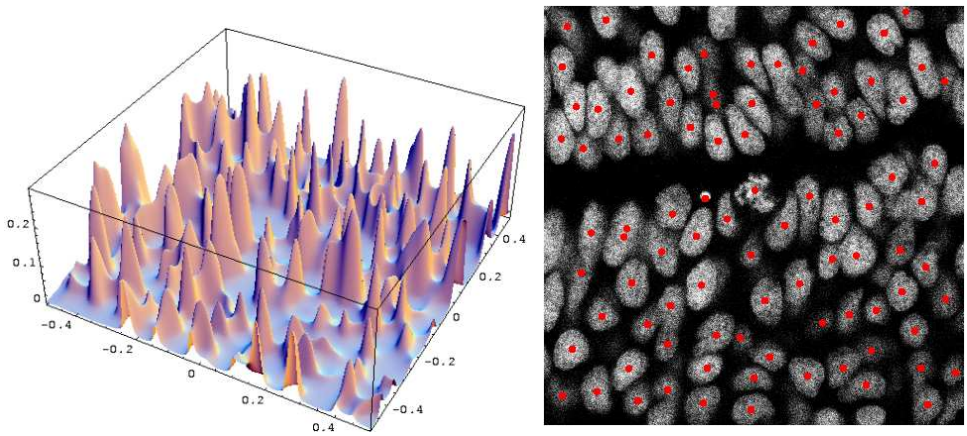


**Fig. 3.** Another example of detecting approximate nuclei centers.

where each slice has a resolution of $512 \times 512$ pixels. One can see approximate nuclei centers superimposed to isosurface visualization of 3D data set in Figure 5. The visual inspection prove that number of found nuclei is very realistic. The parameters of the method were $\delta = 1$, $\mu = 0.00125$, $\varepsilon = 10^{-3}$, $\tau = 0.00125$ and it was stopped after 26 steps.

## 3. CELLS SEGMENTATION

Let us assume that $s_i \in \mathbb{R}^2$ (or $\mathbb{R}^3$), $i = 1, \ldots, S$ are the approximate cell centers which have been detected. We start the cell segmentation first constructing the initial segmentation function given as a peak centered in a "focus point" (one of detected approximate cell centers) inside the segmented cell. Such function can be described at a circle with center $s_i$ and radius $R_i$ by $u_i^0(x) = \frac{1}{|x-s_i|+v}$, where $s_i, i = 1, \ldots, S$ is the focus point and $\frac{1}{v}$ gives maximum of $u_i^0$, e. g. $v = 1$. Outside the circle we take value $u_i^0$ equals to $\frac{1}{R_i+v}$. The choice of $R_i$ depend on estimate how large is a segmented cell. That can also restrict computation to a small image subdomain and consequently speed up computation.

Then the initial function of every cell is evolved numerically solving equation (3) using the semi-implicit co-volume subjective surface method described in Appendix. By the model equation, the solution evolves to a "piecewise constant steady state" which gives the result of the segmentation process. As the criterion to recognize the "steady state" we check whether squared $L_2$ norm of difference in solution between subsequent time steps is less than a threshold $\delta$. Reasonable choice of $\delta = 10^{-5}$ and then our numerical scheme yields the segmentation results in few tens of time steps. In Figure 6 we show 2D example of cell segmentation of the image presented in Figure 1. We show four final "steady states" of the solution to equation (3). To extract the cell shapes we take level line of the final segmentation function which is slightly

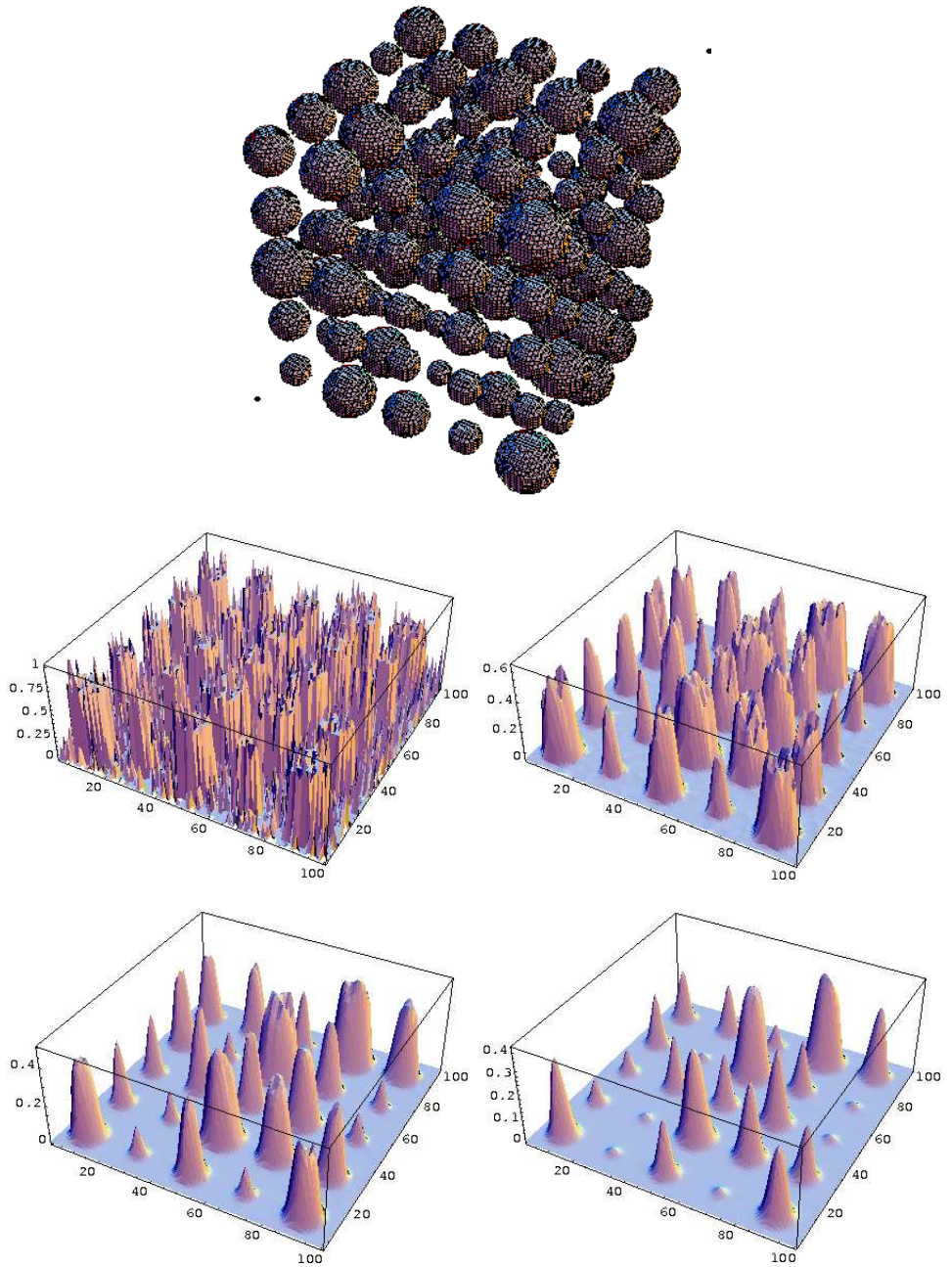


**Fig. 4.** Testing 3D example with 125 spheres of random radii (top), and graphs of image intensity in the central slice at time 0 (middle left) and after 10 time steps (middle right), 20 time steps (bottom left), 30 time steps (bottom right), the process was stopped after 55 time steps when exactly 125 spheres were detected.

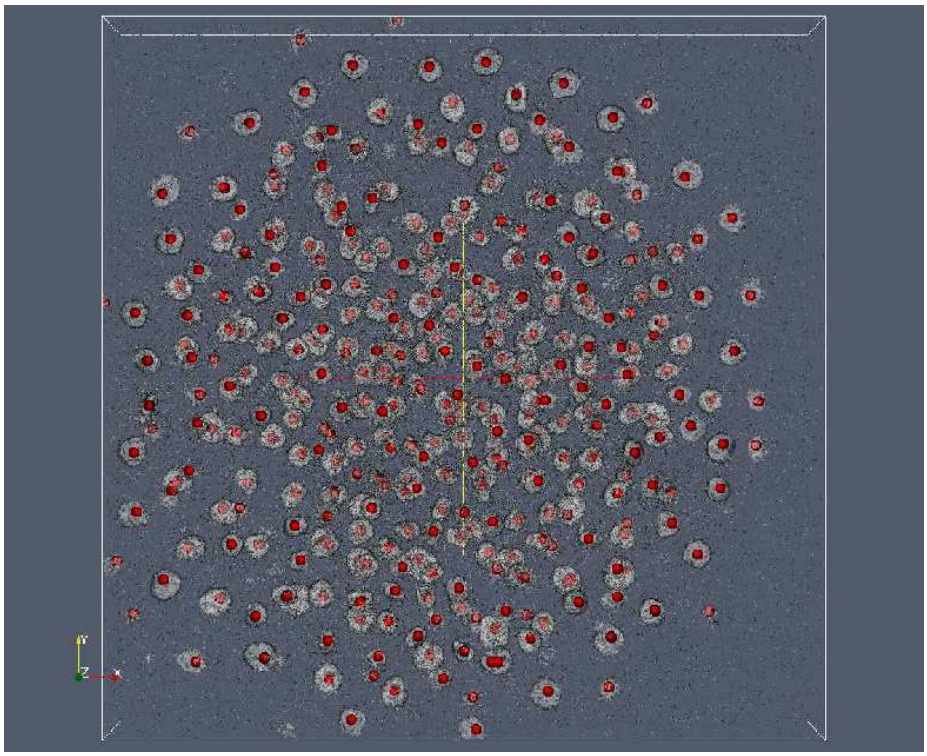

**Fig. 5.** Detection of nuclei centers in 3D embryogenesis image.

bellow its maximum and we superimpose those level-lines onto the membranes image for several cells. In 3D case one can use the same strategy, cf. [1].

## 4. COMPUTATIONAL METHODS

Both equations (2), (3) are considered in a polygonal (image) domain $\Omega \subset \mathbb{R}^d$, $d = 2$ or $d = 3$, and in a time interval $[0, T]$. In case of equation (2) we consider zero Neumann boundary condition at $\partial\Omega$ while for (3) we prescribe zero Dirichlet boundary condition. We assume that a *finite volume mesh* of polygonal subsets $\Omega_i \subset \Omega$, $i = 1, \ldots, I$ is given that covers $\Omega$, i. e.,

$$\overline{\Omega} = \bigcup_{i=1}^{I} \overline{\Omega}_i\,, \quad \Omega_i \neq \emptyset\,, \quad \Omega_i \cap \Omega_j = \emptyset\,, \text{ if } i \neq j\,, \tag{4}$$

and let $\vec{n}_i = \vec{n}_i(\gamma)$ is the outward unit normal vector to $\partial\Omega_i$. In our image processing application the polygonal mesh corresponds simply to image pixel/voxel structure and the finite volumes are given as pixels/voxels of the image. The time interval is also split into (uniform) subintervals $[t^n\,, t^{n+1}], n = 0, 1, \ldots,$ with time step $\tau :=$

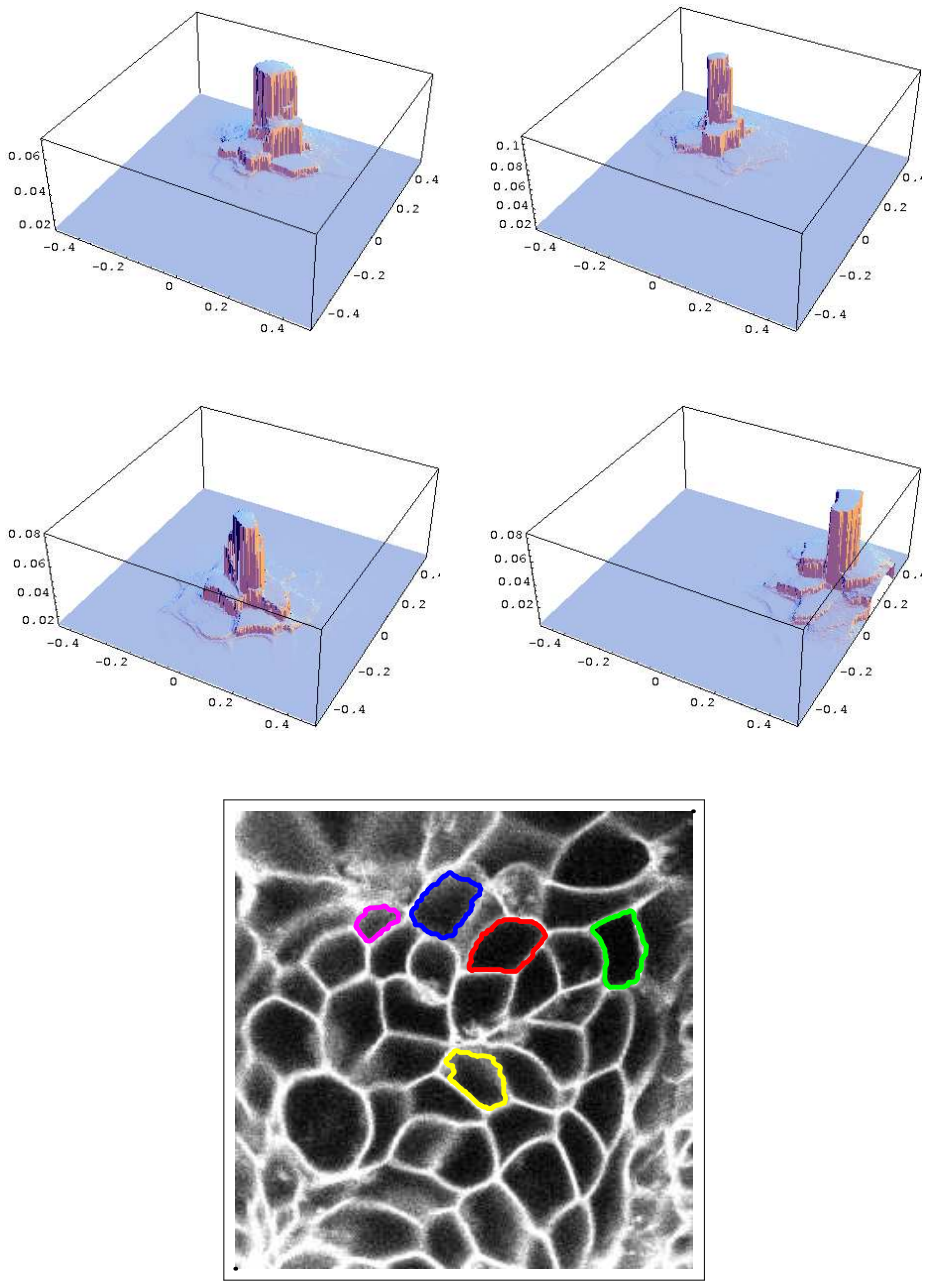

**Fig. 6.** Segmentation of the cells in membranes image of embryogenesis. In the top we see final states of segmentation function for four segmented cells. In the bottom we see several contours representing segmented cells boundaries (including four from above).

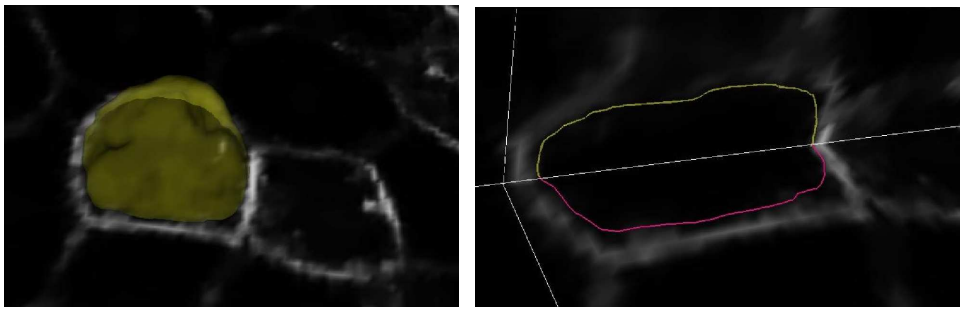

**Fig. 7.** Segmentation of the cell from 3D image of embryogenesis. On the left we plot the isosurface representing the cell superimposed to the $x-y$ image intensity slice, on the right we show the cuts of the isosurface (two isocontours) together with image intensity in the $x-y$ and $x-z$ cutting planes.

$t^{n+1}-t^n$. One can split the boundary $\partial\Omega_i$ to several segments $\Gamma_{ij}$,

$$\partial\Omega_i := \bigcup_{j\in\Lambda_i} \overline{\Gamma_{ij}}\,, \quad \Gamma_{ij} := \partial\Omega_i \cap \partial\Omega_j\,, \tag{5}$$

where the set $\Lambda_i$ contains the indices of neighbouring cells $\Omega_j$ of $\Omega_i$ with $\Gamma_{ij}$ having a nonzero measure in $\mathbb{R}^{d-1}$. To introduce the finite volume discretization of (2), we define the velocity field $\vec{v} = -\delta\,\frac{\nabla u}{|\nabla u|}$ and the integrated fluxes

$$v_{ij} := \int_{\Gamma_{ij}} \vec{n}_i(\gamma)\cdot\vec{v}(\gamma)\,\mathrm{d}\gamma\,, \tag{6}$$

and distinguish between the outflow and inflow boundaries $\Gamma_{ij}$ of $\partial\Omega_i$ by defining the sets of indices $\Lambda_i^{out} := \{j\in\Lambda_i\,,\, v_{ij} > 0\}\,, \quad \Lambda_i^{in} := \{j\in\Lambda_i\,,\, v_{ij}\le 0\}$. Integrating the advective part $\partial_t u + \vec{v}\cdot\nabla u = 0$ of equation (2), considering a piecewise constant approximation $u_i^n$ of $u$ in finite volumes $\Omega_i$ and time intervals $[t^n\,,\,t^{n+1})$, applying the upwind principle and the Green formula we get following finite volume scheme

$$u_i^{n+1}|\Omega_i| = u_i^n\,(|\Omega_i| - \tau v_i) + \sum_{j\in\Lambda_i^{in}} u_j^n\,\tau v_{ji}\,, \tag{7}$$

with $v_i := \sum_{j\in\Lambda_i^{in}} v_{ji}$ denoting the total inflow flux.

For numerical solution of the diffusive part $\partial_t u = \mu|\nabla u|\nabla\cdot\left(\frac{\nabla u}{|\nabla u|}\right)$ of (2) as well as for the evaluation of velocity field $\vec{v}$ in advective part and in discretization of the subjective surface segmentation equation we use the so-called complementary volume (co-volume) technique, see e. g. [3, 4], which is used to construct the finite volume mesh from a finite element (FE) grid. Let $T^e \subset \Omega$, $e = 1,\ldots,E$ be a mesh of finite elements for $\Omega$ (with the properties analogous to (4)), and let $x_i$, $i = 1,\ldots,I$ be the vertices of this grid. Further, let $N_i = N_i(x)$ be the standard

continuous finite element test functions that are polynomial for $x \in T^e$ and that fulfill $N_i(x_j) = \delta_{ij}$. In such a way, the FE interpolation $\hat{u}(t^n, x)$ of the values $u_i^n$ can be defined, $\hat{u}(t^n, x) := \sum_{i=1}^{I} u_i^n N_i(x)$, and the gradient of $\hat{u}(t^n, x)$ is well defined for $x \in T^e$ and is given by $\nabla\hat{u}(t^n, x) = \sum_{k\in\Lambda^e} u_k^n \nabla N_k(x)$ where the set $\Lambda^e$ contains all indices $k$ such that $x_k \in T^e$. The complementary mesh of finite volumes (co-volumes) that fulfills (4) can be constructed by defining $\Omega_i$ around each vertex $x_i$. There exists some freedom in the construction of such vertex-centered finite volumes, but the most common choice is the so called barycenter-based finite volumes. In 2D, they are obtained by connecting the edge-midpoints of elements with the barycenter of elements, and, analogically in 3D case. In our image processing applications with rectangular pixels/voxels, the pixel/voxel centers correspond to the vertices of the finite element grid and co-volumes constructed in such way around the vertices correspond to pixel/voxel image structure. Let indices $e \in \Lambda^{ij}$ denote all elements $T^e$ that contain the vertices $x_i$ and $x_j$. Then, the boundary $\partial\Omega_i$ of co-volume has the form

$$\partial\Omega_i := \bigcup_{j\in\Lambda_i} \bigcup_{e\in\Lambda^{ij}} \overline{\Gamma_{ij}^e}, \quad \Gamma_{ij}^e := \partial\Omega_i \cap \partial\Omega_j \cap T^e . \tag{8}$$

We use the following notation for the gradient of $u$ at $x_{ij} \in T^e$, $x_{ij} := 0.5(x_i + x_j)$,

$$\nabla^e u_{ij}^n := \nabla\hat{u}^n|_{T^e}(x_{ij}) , \tag{9}$$

and we define an approximate average gradient of $u$ in a co-volume by

$$|\nabla u_i^n| := \frac{1}{|\Omega_i|} \sum_{j\in\Lambda_i} \sum_{e\in\Lambda^{ij}} \frac{|\Omega_i \cap T^e|}{2} |\nabla^e u_{ij}^n|. \tag{10}$$

Integrating equation (2) in the finite volume $\Omega_i$, and using the Green theorem, (9), (10) and semi-implicit treatment of time stepping (which means that the nonlinear terms are evaluated from the old time step while linear terms are taken on the new time level), we end up with the following co-volume discretization scheme of diffusive part

$$u_i^{n+1}|\Omega_i| + \tau\ \mu\ |\nabla u_i^n| \sum_{j\in\Lambda_i} \sum_{e\in\Lambda^{ij}} |\Gamma_{ij}^e| \frac{\vec{n}_{ij}^e \cdot \nabla^e u_{ij}^{n+1}}{|\nabla^e u_{ij}^n|} = u_i^n|\Omega_i| \ , \tag{11}$$

where $\vec{n}_{ij}^e$ denotes the outer unit normal to $\Gamma_{ij}^e$. Using boundary conditions, (11) represents a linear system of equations which can be solved efficiently and for which the discrete minimum-maximum principle is valid for our type of rectangular grids and any length of time step $\tau$.

Since the discretization of the advective and diffusive parts of the level set equation (2) can be realized on the same finite volume mesh given by the co-volume method they are easy to combine. Such combination can be straightforwardly explained using the operator splitting procedure. The first step consists in solving the advective part for a given result at time $t^n$. The second step is realized afterwards by taking the result of the first step and solving the diffusive part of (2). In such a

way we get the *flux-based level set method* [3]

$$u_i^{n+1}|\Omega_i| + \tau\mu|\nabla u_i^n| \sum_{j\in\Lambda_i}\sum_{e\in\Lambda^{ij}} |\Gamma_{ij}^e| \frac{\vec{n}_{ij}^e \cdot \nabla^e u_{ij}^{n+1}}{|\nabla^e u_{ij}^n|} = u_i^n|\Omega_i| + \tau \sum_{j\in\Lambda_i^{in}} u_j^n\, v_{ji}^n - \tau v_i^n u_i^n\,,$$

where $v_{ij}^n$ and $v_i^n$ are computed using $\vec{v}(x) = -\delta\, \frac{\nabla \hat{u}^n(x)}{|\nabla \hat{u}^n(x)|}$, and the Evans and Spruck regularization $|s| \approx \sqrt{\varepsilon^2 + |s|^2}$ is used in denominators.

Using the same strategy as deriving (11) we get the *semi-implicit co-volume subjective surface method* [1] for approximation of equation (3)

$$u_i^{n+1}|\Omega_i| + \tau\ \sqrt{\varepsilon^2 + |\nabla u_i^n|} \sum_{j\in\Lambda_i}\sum_{e\in\Lambda^{ij}} |\Gamma_{ij}^e| g(|\nabla^e I_{ij}|) \frac{\vec{n}_{ij}^e \cdot \nabla^e u_{ij}^{n+1}}{\sqrt{\varepsilon^2 + |\nabla^e u_{ij}^n|}} = u_i^n|\Omega_i|\ \,,$$

where $I$ is a finite element interpolation of nodal values of $G_\sigma * u_m^0$ taken in pixel/voxel centers. From Dirichlet boundary condition, the above scheme again represents a uniquely solvable linear system of equations for which the discrete minimum-maximum principle is valid for our type of rectangular grids and any length of time step $\tau$ and which can be solved efficiently using preconditioned linear iterative solvers.

## ACKNOWLEDGEMENT

This work was supported by the European projects Embryomics and BioEmergencies and by the VEGA 1/3321/06 and APVV-RPEU-0004-06 grants. We thank all the members of the Embryomics and BioEmergences projects for our very fruitful interdisciplinary interaction, particularly to Olga Drblíková and Mariana Remešíková for running 3D computations and providing 3D visualizations.

(Received November 30, 2006.)

## REFERENCES

[1] S. Corsaro, K. Mikula, A. Sarti, and F. Sgallari: Semi-implicit co-volume method in 3D image segmentation. SIAM J. Sci. Comput. *28* (2006), 6, 2248–2265

[2] L. C. Evans and J. Spruck: Motion of level sets by mean curvature I. J. Differential Geom. *33* (1991), 635–681.

[3] P. Frolkovič and K. Mikula: Flux-based level set method: A finite volume method for evolving interfaces. Appl. Numer. Math. (2007), doi:10.1016/j.apnum.2006.06.002

[4] A. Handlovičová, K. Mikula, and F. Sgallari: Semi-implicit complementary volume scheme for solving level set like equations in image processing and curve evolution. Numer. Math. *93* (2003), 675–695.

[5] K. Mikula, A. Sarti, and F. Sgallari: Co-volume method for Riemannian mean curvature flow in subjective surfaces multiscale segmentation. Comput. Visual. Sci. *9* (2006), 23–31.

[6] K. Mikula, A. Sarti, and F. Sgallari: Semi-implicit co-volume level set method in medical image segmentation. In: Handbook of Biomedical Image Analysis: Segmentation and Registration Models (J. Suri et al., eds.), Springer, New York, 2005, pp. 583–626.

[7] S. Osher and J. Sethian: Fronts propagating with curvature dependent speed: algorithm based on Hamilton–Jacobi formulation. J. Comput. Phys. *79* (1988), 12–49.
[8] A. Sarti, R. Malladi, and J. A. Sethian: Subjective Surfaces: A Method for Completing Missing Boundaries. Proc. Nat. Acad. Sci. U. S. A. *12* (2000), 97, 6258–6263.
[9] A. Sarti and G. Citti: Subjective surfaces and Riemannian mean curvature flow of graphs. Acta Math. Univ. Comenian. *79* (2001), 1, 85–104.

*Peter Frolkovič, IWR, University of Heidelberg, Im Neuenheimer Feld 368, 69120 Heidelberg. Germany.*
*peter.frolkovic@gmail.com*

*Karol Mikula, Department of Mathematics, Slovak University of Technology, Radlinského 11, 813 68 Bratislava. Slovak Republic.*
*mikula@math.sk*

*Nadine Peyriéras, CNRS-DEPSN, Institut de Neurobiologie Alfred Fessard, Batiment 32-33, Avenue de la Terrasse, 91198 Gif sur Yvette. France.*
*nadine.peyrieras@iaf.cnrs-gif.fr*

*Alessandro Sarti, DEIS, University of Bologna, Via Risorgimento 2, 40136 Bologna. Italy.*
*asarti@deis.unibo.it*